Available online at www.sciencedirect.com
ScienceDirect
Journal of Power Sources 162 (2006) 553–562
JOURNAL OF POWER SOURCES
www.elsevier.com/locate/jpowsour

Performance predictions of a tubular SOFC operating on a partially reformed JP-8 surrogate

Gaurav K. Gupta [a], Jonathan R. Marda [a], Anthony M. Dean [a,*], Andrew M. Colclasure [b], Huayang Zhu [b], Robert J. Kee [b]

[a] *Chemical Engineering Department, Colorado School of Mines, Golden, CO 80401, USA*
[b] *Engineering Division, Colorado School of Mines, Golden, CO 80401, USA*

Received 11 May 2006; received in revised form 8 June 2006; accepted 9 June 2006
Available online 31 July 2006

Abstract

This paper uses chemically reacting flow models to explore the effect of upstream JP-8 steam reforming on the performance of a tubular, anode-supported, solid-oxide fuel cell. In all cases studied in this paper, a steam–carbon ratio of 3 is used for the reformer inlet. However, by varying the reformer temperature, the methane concentration in the reformate stream can be varied. In this study methane mole fractions are varied between 0 and 20%, on a dry basis. The methane mole fraction is found to have a substantial effect on fuel-cell efficiency, power density, and heat-release profiles. The paper also explores the effects of internal reforming chemistry and electrochemical charge transfer on the gas-phase kinetics and propensity for deposit formation. A detailed reaction mechanism is used to describe methane steam reforming on Ni within the anode, while a detailed gas-phase mechanism is used to predict the gas-phase composition in the fuel channel.

Keywords: JP-8; Reforming; SOFC; Efficiency; Deposits

1. Introduction

Solid-oxide fuels cells (SOFC) can use hydrocarbon fuels directly [1–12]. However, practical design and operation require the circumvention of deleterious carbon deposits. In the high-temperature SOFC environment, carbon deposits can be formed via two mechanisms [9,13]. Coke formation on catalysts such as Ni, Fe, and Co is well known [14,15]. This process generally involves the adsorption of a carbon source onto the metal surface, dissolution of the carbon into the bulk of the metal, and finally precipitation of carbon as a graphite fiber. Gas-phase reactions can also produce higher-molecular weight species, e.g., aromatics, which can serve as deposit precursors [16]. These reactions are most important for hydrocarbons larger than methane and are usually initiated by C–C bond scission at high temperatures.

Most SOFC systems are designed to reform the hydrocarbon fuel upstream of the fuel cell itself [17,18]. Following reformation, either by steam reforming or catalytic partial oxidation (CPOX), the fuel that enters the fuel cell is primarily H_2, CO, and possibly CH_4. There is also active development of systems to enable deposit-free reforming or partial oxidation within the SOFC anode structure [11,19–21].

There can be substantial advantages to carrying hydrocarbons into the SOFC itself, as long as deposits can be avoided. Reducing the amount of upstream reforming contributes to overall higher system efficiency. Hydrocarbon reforming within the stack can also assist thermal management. Excess heat generated by inefficiencies within the cell is used directly to support endothermic steam-reforming chemistry.

This paper focuses on the impact of external steam reforming of JP-8 on SOFC performance. Depending on the reformer temperature, the reformate stream is primarily a mixture of CO, H_2, CO_2, H_2O and varying amounts of CH_4. Increasing the CH_4 fraction can increase the fuel-cell efficiency and can improve thermal management. The paper uses a computational model to predict fuel-cell performance as a function of the CH_4 fraction in the reformate stream. Performance measures include efficiency, power density, and heat-source profiles.

Several coupled models are used in this study. The upstream steam reformer is assumed to operate at chemical equilibrium.

* Corresponding author. Tel.: +1 303 273 3643; fax: +1 303 273 3730.
E-mail address: amdean@mines.edu (A.M. Dean).

0378-7753/$ – see front matter © 2006 Elsevier B.V. All rights reserved.
doi:10.1016/j.jpowsour.2006.06.041

Thus, the reformate outlet stream depends on the inlet steam–carbon ratio and the reformer temperature. The *fuel-cell model* incorporates fluid flow in the fuel channel, porous-media transport within the electrodes, heterogeneous reforming chemistry, and electrochemical charge transfer [22]. This model considers major gas-phase species, but owing to computation cost, cannot handle the hundreds of species and thousands of reactions needed to model the gas-phase kinetics leading to polyaromatic hydrocarbon deposits. Therefore, a *fuel-channel model* is developed to model this complex homogeneous chemistry. The fuel-cell model and the fuel-channel model must be coupled through the species flux exchanged between the fuel channel and the anode structure.

The models require chemical reaction mechanisms to describe chemical kinetics at various levels of complexity. Catalytic steam reforming on Ni within the anode is incorporated into the fuel-cell model using a detailed reaction mechanism described by Hecht et al. [23]. The elementary gas-phase reaction mechanism used in the fuel-channel model is described by Gupta et al. [24]. This is a large mechanism that represents the kinetics of molecular-weight growth, including polyaromatic hydrocarbons. A much smaller gas-phase mechanism is also developed and used to assist understanding the impact of the gas-phase chemistry on the catalytic reactions within the anode.

2. Model descriptions

Fig. 1 illustrates an anode-supported, tubular, cell with an internal fuel feed. Although the models are general, the results discussed in this paper consider a particular geometry and membrane electrode assembly (MEA) structure. The fuel-feed tube has inner and outer diameters of 0.36 and 0.6 cm, respectively, yielding a 0.1 cm^2 cross-sectional flow area. The inner diameter of the anode structure is 1 cm, yielding an annulus cross-sectional area of 0.5 cm^2 for the fuel flow. The anode support is 1.2 mm thick and the tube is 60 cm long.

Table 1
Parameters for an SOFC MEA structure

Parameters	Value	Units
Anode		
Thickness (L_a)	1220	μm
Porosity (ϕ_g)	0.35	
Tortuosity (τ_g)	3.50	
Average pore radius (r_p)	0.50	μm
Average particle diameter (d_p)	2.50	μm
Specific catalyst area (A_s)	1080	cm^{-1}
Cathode		
Thickness (L_c)	30	μm
Porosity (ϕ_g)	0.35	
Tortuosity (τ_g)	3.50	
Average pore radius (r_p)	0.5	μm
Average particle diameter (d_p)	2.5	μm
Electrolyte: $\sigma_{el} = \sigma_0 T^{-1} \exp(-E_{el}/RT)$		
Thickness (L_{el})	25	μm
Activation energy of O^{2-} (E_{el})	8.0E4	J mol^{-1}
Pre-factor of O^{2-} (σ_0)	3.6E5	S-K/cm
Leakage overpotential (η_{max})	0.055	V
Leakage overpotential (i_{max})	8.0	A cm^{-2}

The MEA is comprised of a 1.2 mm thick Ni-YSZ anode support, 25 μm thick dense yttria-stabilized zirconia (YSZ) electrolyte, and a 30 μm thick strontium-doped lanthanum manganite (LSM) cathode. This MEA structure is based on the button-cell structure reported by Jiang and Virkar [25], and the physical parameters are shown in Table 1. Complete details of the modeling parameters are reported and discussed in Zhu et al. [22].

As illustrated in Fig. 1, current collection on the cathode side can be accomplished by wrapping wires around the outer diameter of the tube. Anode current collection is more difficult in a tubular cell. The Ni-YSZ is electrically conductive, so there

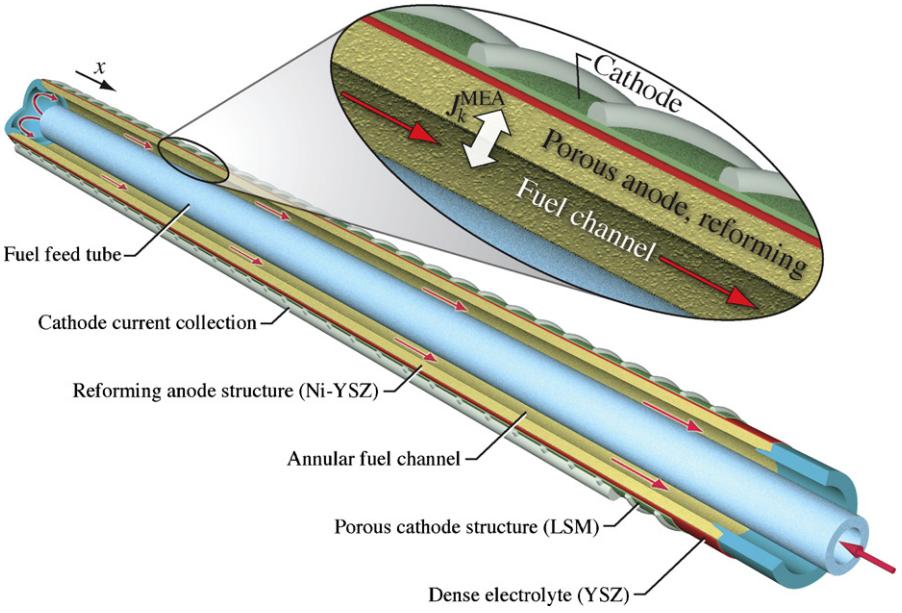

Fig. 1. An anode-supported tubular solid oxide fuel with a central fuel feed tube.

can be axial current flow through the support structure. However, for a long cell as considered here, the axial voltage drop is far too great to be practical. The results shown in this paper assume that the operating cell potential is uniform throughout the cell. Thus, some effective approach for anode current collection is required, but is not discussed here.

2.1. Fuel-cell model

The fuel-cell model is derived and discussed in great detail by Zhu et al. [22]. Briefly, the model considers plug flow in the fuel channel, Dusty-Gas transport in the porous electrode structures, elementary reforming chemistry on Ni, charge-transfer reactions in a modified Butler–Volmer form, and oxygen ion transport through the dense electrolyte. Zhu et al. [22] also discuss the physical and chemical parameters that are used to represent the particular MEA that is used in the present paper. These parameters are determined by fitting a model to the button-cell data reported by Jiang and Virkar [25].

The heterogeneous reaction mechanism that describes reforming kinetics within the Ni-YSZ anode taken from Hecht et al. [23]. This mechanism has been validated experimentally for both steam and dry (CO_2) reforming within a Ni-YSZ anode at 800 °C. The mechanism involves 42 irreversible reactions among 6 gas-phase and 12 surface-adsorbed species.

Modeling the tubular cell in the present paper requires two relatively straightforward modifications of the model developed by Zhu et al. [22], which considers a defined-channel, planar, cell architecture. Thus, the porous-media transport within electrodes must be recast in radial coordinates. Because the Dusty-Gas model is derived in a general vector setting, the conversion to cylindrical coordinates is straightforward. In the tubular geometry there is no air-flow channel on the cathode side. Rather, the entire exterior surface of the tube is exposed to air. The results in this paper assume undiluted air everywhere on the cathode that forms the tube exterior surface.

2.2. Fuel-channel model

A fuel-channel model is developed to explore gas-phase kinetics in the fuel channel. The steady-state, isothermal, mass-balance equations that describe the overall and species continuity in the fuel channel are:

$$\frac{\mathrm{d}(\rho u)}{\mathrm{d}x} = \frac{P}{A_c}\sum_{k=1}^{K_g} J_k^{\mathrm{MEA}} W_k, \tag{1}$$

$$\frac{\mathrm{d}(\rho u Y_k)}{\mathrm{d}x} = \frac{P}{A_c} J_k^{\mathrm{MEA}} W_k + \dot{\omega}_k W_k, \tag{2}$$

$$\rho = \frac{p}{RT}\frac{1}{\sum Y_k / W_k}. \tag{3}$$

The independent variable x is the distance along the annular fuel channel. The dependent variables are the mean fluid velocity u and the species mass fractions Y_k. The mass density ρ is determined from a perfect-gas equation of state. The species molecular weights are W_k. The species molar production rates by homogeneous reaction are represented as $\dot{\omega}_k$. The annular channel geometry is characterized by the outer perimeter P (perimeter of the inner surface of the anode structure) and flow cross-sectional area (formed between the outer surface of the feed tube and the inner surface of the anode structure).

The variables J_k^{MEA} represent the molar species fluxes between the fuel-flow channel and the inner surface of the anode structure. These fluxes are the result of electrochemistry in the three-phase region near the dense electrolyte, thermal heterogeneous chemistry within the porous anode structure, and porous-media species transport. The spatial profiles of $J_k^{\mathrm{MEA}}(x)$ are determined by the fuel-cell model, and supplied as external functions to the fuel-channel model. This flux exchange is referenced to the inner anode surface area (i.e., the outer wall of the annular flow channel).

Eqs. (1) and (2) are a coupled system of ordinary differential equations, which can be solved to determine the velocity and composition profiles along the channel length. The species production rates $\dot{\omega}_k$ depend on an elementary reaction mechanism, which is evaluated through a CHEMKIN interface [26]. This stiff initial-value problem is solved using the DVODE software [27].

The elementary gas-phase reaction mechanism used in this paper is an extension of one used earlier to describe butane pyrolysis [16]. The mechanism, which involve some 350 species and 3450 reactions, represents oxidation and pyrolysis kinetics for hydrocarbons up to C6. It also includes the molecular-weight-growth reactions leading to polyaromatic hydrocarbon (PAH) formation. The detailed mechanism[1] is described in our earlier work [24], where it was used to explore methane oxidation and pyrolysis under SOFC operating conditions.

3. Steam reforming of JP-8

Steam reforming of JP-8 is assumed to be an equilibrium process. JP-8 typically consists of 80.1% alkanes with between 10 and 15 carbon atoms, 1.9% olefins, and 18% aromatics. Since the equilibrium composition at a given temperature is completely specified by the atomic composition, it is sufficient to consider a surrogate mixture that corresponds to the carbon/hydrogen ratio of JP-8. Specifically, we use a surrogate mixture containing 80.1% $C_{13}H_{28}$, 1.9% $C_{13}H_{26}$ and 18% propyl naphthalene ($C_{13}H_{14}$). Throughout this paper, we use a steam-to-carbon ratio of 3 (S/C = 3). Table 2 shows the mixture composition at S/C = 3 which enters the reformer.

Table 2
Jet fuel (JP-8) surrogate and steam mixture composition corresponding to S/C = 3

Species	Molar%	Mass%
$C_{13}H_{14}$	0.45	3.46
$C_{13}H_{26}$	0.05	0.42
$C_{13}H_{28}$	2.00	16.66
H_2O	97.50	79.46

[1] The mechanism and the associated thermodynamic database are available upon request.

Table 3
Measured [28] and calculated equilibrium mole fractions (dry basis) for steam reforming of JP-8 at 512 °C, atmospheric pressure, and S/C = 3

Species	Measured	Equilibrium
CH_4	0.14	0.16
CO	0.03	0.03
CO_2	0.23	0.23
H_2	0.60	0.58

Although we assume equilibrium production at a constant reformer temperature, we recognize that actual operation of a JP-8 reformer under these conditions requires careful attention to details (e.g., fuel desulphurization to avoid catalyst deactivation and a reactor designed to achieve high heat transfer rates). Nevertheless, the equilibrium assumption is a convenient starting point for analysis and there is evidence that it is possible to run actual reformers under conditions that closely approach equilibrium. For example, Strohm et al. [28] have measured the products of JP-8 steam reforming at S/C = 3. They report results at a reformer temperature of 512 °C over a catalyst composed of 2% Rh and 10% Ni supported on CeO_2–Al_2O_3. Table 3 shows the measured product distribution and the equilibrium mole fractions. It is evident that the equilibrium predictions are comparable to the experimental values.

Selecting steam-reformer operating conditions depends primarily on two considerations. One is deposit formation in the reformer and the other is the desired CH_4 fraction in the reformate. The operating conditions are specified primarily as the steam–carbon ratio (S/C) and reformer temperature.

The propensity for carbon deposition can be estimated by calculating the equilibrium solid graphite fraction as a function of temperature and mixture atomic composition. Fig. 2 is a ternary diagram that summarizes the equilibrium states. Equilibrium graphite exists in the regions above the isotherm lines, whereas the mixtures are entirely gas phase below the isotherms. Two dots on the chart show the composition of JP-8 and a mixture of JP-8 and steam at S/C = 3. The S/C = 3 mixture indicates no deposits at the relatively low temperature of 493 °C, suggesting that a reformer could be operated under these conditions without deposit formation.

The reformer temperature has a strong influence on the CH_4 fraction in the reformate. Table 4 shows reformate composition at five different temperatures, which are chosen to deliver up to 20% methane (on a dry basis). The right-hand columns of Table 4 show the heats of reaction ΔH and free-energies ΔG associated with complete oxidation of 1 mol of the reformate *at the fuel-cell temperature* of 800 °C.

Although the inlet mixture to the reformer is the same in all cases, it is evident that ΔH and ΔG of the resulting reformate streams are very different. As the reformer temperature decreases, a larger fraction of the hydrogen is contained in CH_4 and less in H_2. This contributes to increases in the heating value ΔH and the free-energy ΔG. Also, the resulting $\Delta G/\Delta H$ ratio for the reformate is higher at lower reformer temperatures, indicating the potential for increased fuel-cell efficiency. It should be noted that different amounts of sensible energy are needed to heat the reformate mixtures from the reformer temperatures to the fuel cell temperature. In all cases, however, essentially the same amount of sensible energy is needed to heat the JP-8–steam mixture from room temperature to reformer temperature, and then to fuel-cell temperature. Of course, different levels of energy input are needed to support the endothermic reforming at different reformer temperatures.

The equilibrium analysis is useful guide for deposit formation, but kinetics often govern deposit formation. Deposits can be observed in the region expected to be deposit-free if the kinetics leading to deposit formation are faster than those removing deposits. For example, Strohm et al. [28] report deposits from JP-8 reforming at S/C = 3 and 512 °C, even though this is not in the region where deposits are anticipated by equilibrium (Fig. 2). Conversely, one might not observe deposits for a composition within the carbon deposit region if the deposit-forming kinetics are slow.

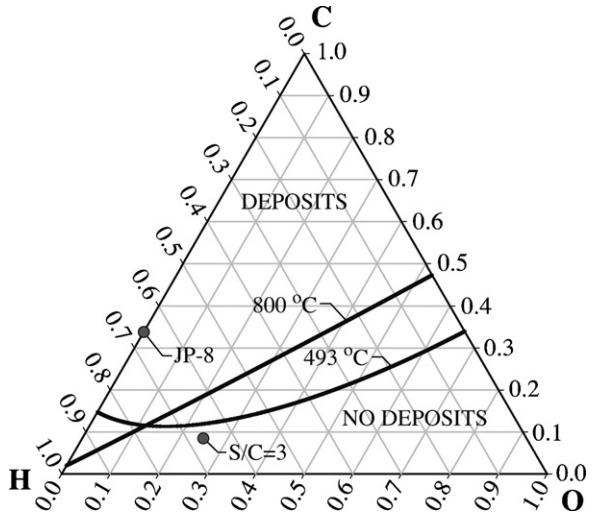

Fig. 2. Ternary C–H–O diagram showing the region where deposits (in the form of graphite) are present at chemical equilibrium.

Table 4
Equilibrium reformate composition (mole fractions) for JP-8–steam mixtures at different reformer temperatures and at S/C = 3

CH_4 mole fraction (dry%)	T (°C)	CH_4	CO	CO_2	H_2	H_2O	ΔH (kJ mol^{-1})	ΔG (kJ mol^{-1})	$\Delta G/\Delta H$
0	690	0	0.097	0.103	0.492	0.308	150	97.2	0.650
5	599	0.033	0.059	0.122	0.447	0.339	154	107	0.696
10	555	0.062	0.036	0.128	0.389	0.385	156	115	0.737
15	521	0.086	0.022	0.127	0.335	0.429	158	122	0.770
20	493	0.106	0.014	0.124	0.286	0.470	160	128	0.797

The heats of reaction ΔH and free-energies ΔG are associated with the complete oxidation of 1 mol of the equilibrium mixtures at 800 °C.

4. Efficiency and power density

To explore the effect of CH_4 fraction on the fuel-cell performance, the mixtures listed in Table 4 are used as input to the fuel-cell model. Table 5 shows predicted efficiency, power density, current density, and net heat release. In all cases, the cell is operated at 800 °C and atmospheric pressure, and the fuel utilization is fixed at 85%. Cell operating potentials of $E_{cell} = 0.8$ and 0.6 V are considered.

Fuel-cell efficiency is determined as,

$$\varepsilon = \frac{W_e}{Q_{in}} = \frac{\int i E_{cell}\, dA}{\dot{m}_{f,in}\Delta h_{in}}, \quad (4)$$

where W_e is the electrical work output and Q_{in} is the heat released upon full oxidation of the inlet fuel stream. The inlet fuel mass flow rate is $\dot{m}_{f,in}$ and Δh_{in} is the specific enthalpy associated with completely oxidizing the fuel stream. The electrical work is the product of the current density i and the operating voltage E_{cell}, integrated over the active MEA area.

The net efficiency can be represented as the product of three contributing efficiencies [29,30]

$$\varepsilon = \varepsilon_R \varepsilon_V \varepsilon_U, \quad (5)$$

where ε_R is the reversible efficiency, ε_V the part-load efficiency, and ε_U is the fuel utilization. The reversible efficiency is determined thermodynamically as

$$\varepsilon_R = \frac{\Delta G}{\Delta H}, \quad (6)$$

where ΔH and ΔG are the heats of reaction and free-energies associated with complete oxidation of the fuel stream. The part-load (or voltage) efficiency is the ratio of the cell operating voltage and the reversible (Nernst) potential as,

$$\varepsilon_V = \frac{E_{cell}}{E_{rev}}. \quad (7)$$

The fuel utilization is written as

$$\varepsilon_U = 1 - \frac{\dot{m}_{f,out}\Delta h_{out}}{\dot{m}_{f,in}\Delta h_{in}}, \quad (8)$$

where the "in" and "out" refer to the inlet and outlet of the fuel cell. The Δh term refers to the specific enthalpy associated with complete oxidation of any available fuel. This definition thus accounts for the energy content of any remaining fuels (or fuel byproducts) that leave in the fuel-cell exhaust.

Table 5 shows that the average efficiency and power density depend substantially on the methane mole fraction and operating potential. Increased CH_4 fraction leads to increased efficiency, primarily due to the increase in the reversible efficiency, $\Delta G/\Delta H$ (see Table 4). These predictions are consistent with the findings of Aguiar et al. [31], who also predict increased efficiency with increasing CH_4.

The effect of operating potential on performance is not monotonic. Zhu and Kee [30] show that efficiency tends to peak at operating potentials around 0.8 V and power densities peak at lower operating potentials around 0.6 V. The results in Table 5 are consistent with these trends, showing much greater power densities at 0.6 V than at 0.8 V. The results also show much greater efficiencies at 0.8 V than at 0.6 V. The decreased efficiency at lower operating potential is the result of the part-load efficiency factor $\varepsilon_V = E_{cell}/E_{rev}$.

Increasing the methane mole fraction causes decreasing current and power densities. Because inefficiencies scale with the current density squared, it should be anticipated that efficiency increases as current density decreases. Indeed this behavior is shown in Table 5. This is also consistent with work of Aguiar et al. [31].

To achieve a constant fuel utilization of 85%, the fuel flow rate must decrease as the methane fraction increases due to the time required for the methane to be reformed and consumed. At $E_{cell} = 0.8$ V, the inlet velocity must be decreased from 210 to 130 cm s^{-1} as the methane mole fraction is increased from 0 to 20%. At $E_{cell} = 0.6$ V, the inlet velocity must be decreased from 635 to 365 cm s^{-1} as the methane mole fraction is increased from 0 to 20%. The decrease in fuel flow rate causes the electrochemical activity to decrease because there is less fuel available per unit time to be electrochemically oxidized. The reduced electrochemical activity lowers the average current density, which lowers the power density at uniform operating potential.

The operating potential affects the current density because the electrochemical driving potential depends on the difference between the reversible and operating potentials. Thus, at 0.6 V, the electrochemical charge-transfer reactions proceed more rapidly, delivering higher current density. This behavior is evident in Table 5, showing much higher current densities at 0.6 V.

In addition to efficiency and power density, local heat-release profiles are also an important performance metric. More uniform heat release is desirable because it leads to more uniform operating temperatures. Fig. 3 shows that as the methane mole fraction increases the local heat-release rates decrease. The heat release is the result of cell inefficiency. As more available heat is used to support internal steam reforming of the methane, less net heat is produced. This also improves efficiency, since otherwise wasted heat is used beneficially to support the needed fuel reforming. At lower operating potential where the efficiency is

Table 5
Efficiency, average power density, and average current density as functions of CH_4 fraction and operating voltage

CH_4 mole fraction (%)	0.8 V			0.6 V		
	Efficiency	Power density (W cm^{-2})	Current density (A cm^{-2})	Efficiency	Power density (W cm^{-2})	Current density (A cm^{-2})
0	0.52	0.40	0.50	0.39	0.89	1.49
5	0.55	0.36	0.45	0.40	0.79	1.31
10	0.57	0.33	0.42	0.42	0.71	1.18
15	0.59	0.32	0.40	0.44	0.66	1.10
20	0.61	0.31	0.38	0.45	0.63	1.06

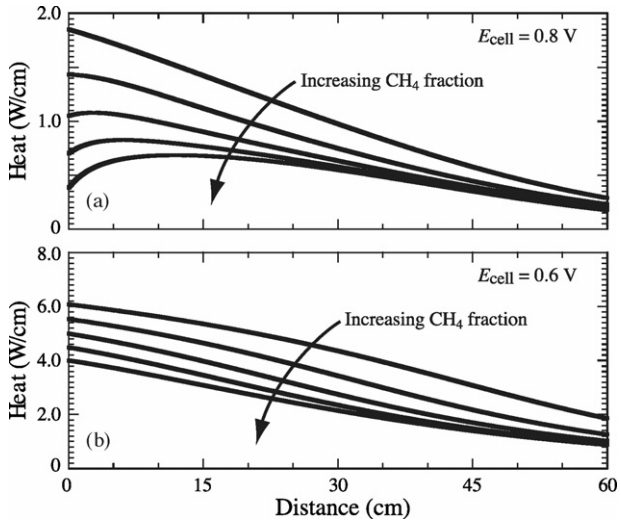

Fig. 3. Heat-release profiles as a function of CH_4 mole fraction at operating potentials of (a) 0.8 V and (b) 0.6 V.

lower, the net heat is substantially greater. It is evident in Fig. 3 that the heat rates are much greater at 0.6 V than at 0.8 V. It is also clear that increasing methane mole fraction in the fuel leads to more spatially uniform heat-release profiles. This is because the electrochemically active H_2 is the result of reforming, which is distributed throughout more of the cell with high methane mole fractions in the fuel stream.

5. Anode species exchange

The species flux between the porous anode and the fuel channel, designated J_k^{MEA} in Eqs. (1) and (2), depends on reforming chemistry within the porous anode and charge-transfer electrochemistry in the three-phase region. In this section, the fuel-cell model is used to predict $J_k^{MEA}(x)$ under four different operating conditions. Then, the fuel-channel model is used to predict the species profiles in the fuel channel. The four cases considered are:

(1) Only gas-phase reactions in the fuel channel. This is a reference case, in which no heterogeneous chemistry or electrochemistry is allowed.
(2) The cell is operated at open-circuit conditions. Reforming may proceed within the anode but there is no electrochemical charge transfer.
(3) The cell is operated at $E_{cell} = 0.8$ V, leading to relatively high efficiency and low power density.
(4) The cell is operated at $E_{cell} = 0.6$ V, leading to relatively low efficiency and high power density.

For cases (3) and (4), the fuel flow rates are adjusted to achieve 85% fuel utilization. The flow rates for cases (1) and (2) are the same as that for case (3).

In principle, the full gas-phase reaction mechanism, including molecular-weight growth chemistry, could be included in the fuel-cell model. However, extraordinarily long computation times render this approach entirely impractical. Thus, the fuel-cell model is exercised with two assumptions about gas-phase chemistry. First, gas-phase chemistry is simply neglected. Second, a reduced mechanism containing 37 species and 150 reactions is included. The reduced mechanism is validated by direct comparison with the full mechanism in a channel with no heterogeneous chemistry or electrochemistry. The major-species profiles are predicted accurately by the reduced model. Moreover, the fuel-cell model results are nearly identical with gas-phase chemistry neglected and with the reduced model. Including the reduced mechanism increases computation time for the fuel-cell model from about 5 min to about 5 h on a personal computer. For the nominal operation conditions here, it is reasonable to neglect gas-phase chemistry for the purposes of predicting major species and cell performance. It should be noted, however, that neglecting gas-phase chemistry may not be valid at higher temperatures, higher pressures, or for fuels containing higher hydrocarbons.

Because catalytic and charge-transfer kinetics determine the species exchange between the anode and the fuel channel, the analysis of gas-phase kinetics can be decoupled as a two-step process:

(1) Apply the fuel-cell model without gas-phase kinetics to obtain the species exchange J_k^{MEA} between anode and fuel channel.
(2) Use the $J_k^{MEA}(x)$ profiles as input to the fuel-channel model, which incorporates the complete gas-phase reaction mechanism.

Fig. 4 shows the flux exchange for the fully reformed case (i.e., 0% CH_4). At OCV and no methane in the fuel, no reforming is possible and the reactions within the anode represent the water-gas-shift process (i.e., $H_2O + CO \rightleftharpoons H_2 + CO_2$). Because the reformer and fuel cell are at different temperatures, the system seeks to adjust to a new equilibrium state at the higher fuel-cell temperature. The new equilibrium is reached by about 15 cm into the channel. The resulting fluxes are very small and are not presented here. Fig. 4 shows the anode flux exchange at operating potentials of $E_{cell} = 0.8$ V and $E_{cell} = 0.6$ V. The H_2 flux is negative (indicating flow into the anode structure) because H_2 is being consumed electrochemically. The positive H_2O and CO_2 fluxes show that the reaction products are being transported from the anode into the fuel channel. The fluxes are higher in the $E_{cell} = 0.6$ V case (Fig. 4b) because the power densities are higher. As the fuel is depleted, the fluxes are generally reduced toward the exhaust end of the cell.

Fig. 5 shows anode flux exchange for the 20% CH_4 mole fraction case. In the OCV case (Fig. 5a), reforming within the anode causes an initial flux of CH_4 and H_2O into the anode, while H_2 and CO flow into the fuel channel. At relatively low current density ($E_{cell} = 0.8$ V, Fig. 5b), the net hydrogen flux is into the anode because of electrochemical consumption. As the current density increases ($E_{cell} = 0.6$ V, Fig. 5c), the fluxes are larger than at low current density. As expected, the net flux of H_2 is into the anode, with product fluxes of H_2O and CO_2 flowing into the channel.

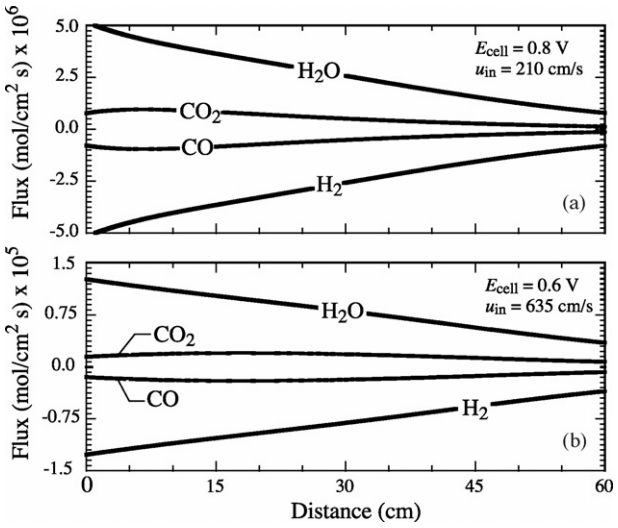

Fig. 4. Major-species flux exchange between the anode structure and the fuel channel at an operating potential of (a) 0.8 V and (b) 0.6 V. The cell is maintained at 800 °C and 1 atm. Inlet fuel composition is 0.0% CH_4, 30.8% H_2O, 49.2% H_2, 10.3% CO_2, and 9.7% CO, corresponding to a 0% CH_4 fraction. Inlet velocities are adjusted to achieve 85% fuel utilization. Note the different ordinate scales in the two panels.

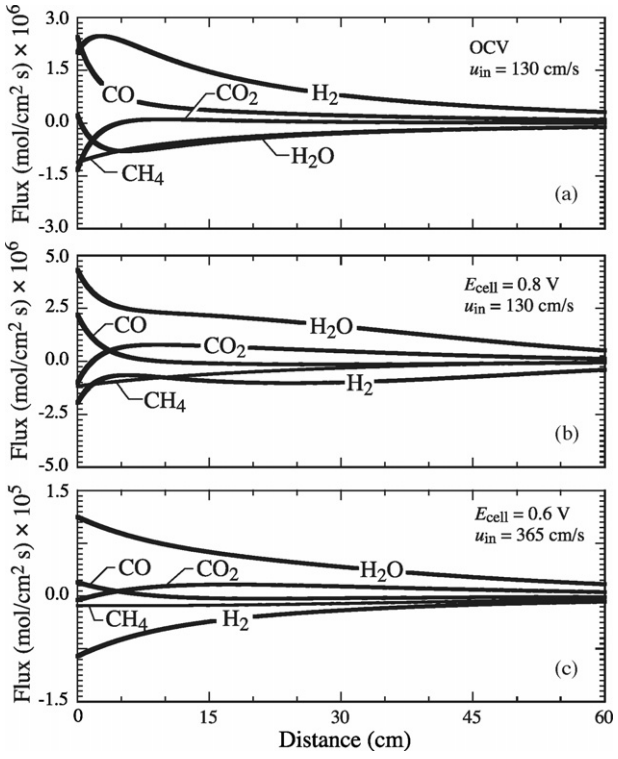

Fig. 5. Major-species flux exchange between the anode structure and the fuel channel at (a) OCV, (b) 0.8 V and (c) 0.6 V. The cell is maintained at 800 °C and 1 atm. Inlet fuel composition is 10.6% CH_4, 47.0% H_2O, 28.6% H_2, 12.4% CO_2, and 1.4% CO, corresponding to a 20% CH_4 fraction. Inlet velocities are adjusted to achieve 85% fuel utilization for cases (b) and (c). Note the different ordinate scales in the lower panel.

6. Fuel-channel composition

Solving Eqs. (1) and (2), using $J_k^{\mathrm{MEA}}(x)$ as input, yields species-composition profiles along the channel. The fuel-channel model now considers a complete gas-phase reaction mechanism. Figs. 6 and 7 show major-species profiles with four different operating conditions. With the chosen inlet conditions, there is no change in the composition of major species within the inner tube. However, small concentration of radicals are produced in this region that may affect the gas-phase kinetics in the outer tube. Thus, in the fuel-channel model we use the radical compositions at the end of the inner tube as an initial condition to predict the mole fraction profiles in the outer tube for all the species in the full mechanism.

Figs. 6a and 7a, which consider only gas-phase chemistry (i.e., no catalytic chemistry or electrochemistry), show that species profiles remain essentially unchanged along the channel. At open-circuit voltage, however, the situation can be quite different because reforming chemistry is active in the anode structure. Fig. 6b shows nearly no chemical activity. Once methane is present, reforming chemistry can proceed even at OCV. Fig. 7b shows that H_2 and CO profiles increase along the channel length as CH_4 reacts with H_2O on the anode catalyst.

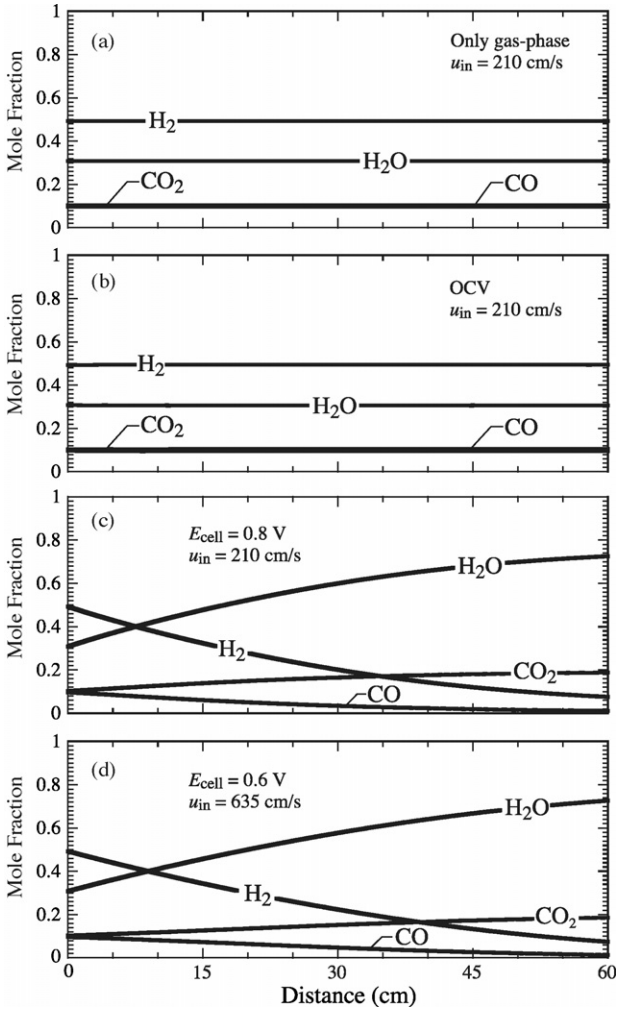

Fig. 6. Major species profiles for an SOFC channel at 800 °C and 1 atm when (a) only gas-phase reactions considered, (b) at OCV, where catalytic reforming also considered, (c) at 0.8 V and (d) 0.6 V. Fuel inlet composition is 0.0% CH_4, 30.8% H_2O, 49.2% H_2, 10.3% CO_2, and 9.7% CO. Inlet velocities are adjusted to achieve 85% fuel utilization for cases (c) and (d). Flow rates for cases (a) and (b) are the same as for case (c).

When the cell is operated under electrical load, H_2 is consumed electrochemically to produce H_2O and CO_2. Figs. 6c and d, and 7c and d show the major-species profiles for two operating potentials and two methane mole fractions in the inlet fuel. It is interesting to note that in Fig. 6c and d, the cell potential has only a minor effect on the species profiles. This is because there is no methane and because the inlet flow rates have been adjusted to achieve 85% utilization in both cases. When methane is present, Fig. 7c and d show that the cell potential has a stronger effect on the species profiles. At $E_{cell} = 0.8$ V, the current density is lower and the H_2 is consumed less rapidly. In addition to less-rapid H_2 consumption at low current density, the production of H_2 by reforming serves to maintain larger H_2 concentrations throughout the channel. At higher current densities, Fig. 7d shows that fuel is depleted faster in the upstream portion of the channel.

These results show that when only gas-phase chemistry is considered, gas-phase chemistry has a negligible effect on major-species profiles. This is because for methane at 800 °C, the initiation reactions are quite endothermic and very slow. However, when catalytic reactions are included within the anode structure, methane reforming chemistry affects the species profiles significantly. When operating the cell under load, the species profiles are affected by a combination of electrochemical charge-transfer and heterogeneous reforming kinetics.

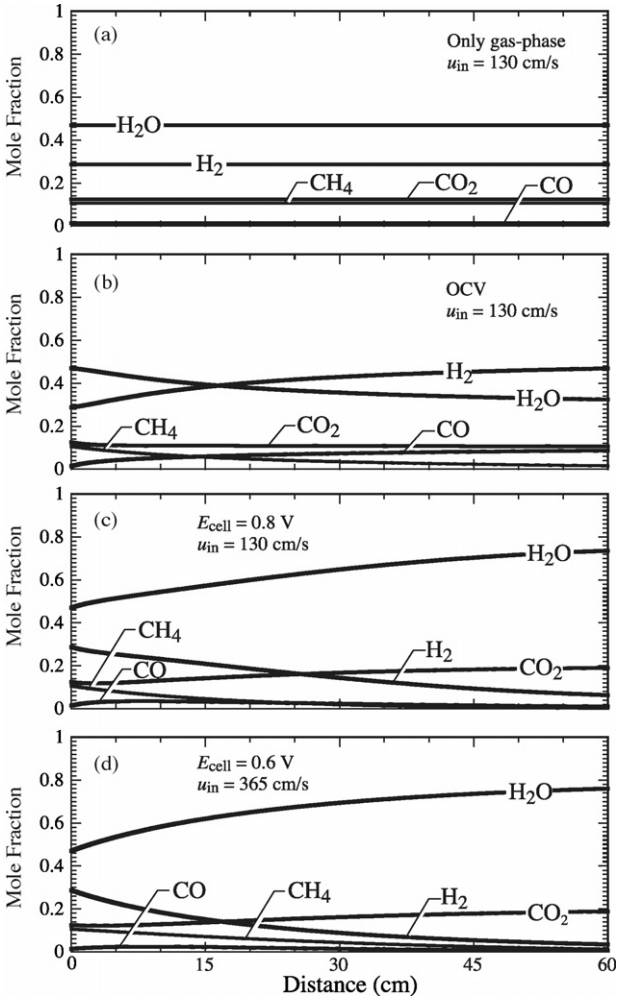

Fig. 7. Major species profiles for an SOFC channel at 800 °C and 1 atm when (a) only gas-phase reactions considered, (b) at OCV, where catalytic reforming also considered, (c) at 0.8 V and (d) 0.6 V. Fuel inlet composition is 10.6% CH_4, 47.0% H_2O, 28.6% H_2, 12.4% CO_2, and 1.4% CO, corresponding to a 20% CH_4 fraction. Inlet velocities are adjusted to achieve 85% fuel utilization for cases (c) and (d). Flow rates for cases (a) and (b) are the same as for case (c).

7. Molecular-weight growth

Although the major species are only weakly affected by gas-phase chemistry, it is interesting to explore minor-species behavior and the potential for carbon deposition via polyaromatic hydrocarbon growth. A rate analysis shows that hydroxyl (OH) and methyl (CH_3) radicals play a critical role in the kinetics of molecular-weight growth. Ethane is formed by the recombination of methyl radicals. Hydrogen abstraction from ethane forms ethyl, which then reacts by beta-scission to form the first unsaturated species (ethylene). Then, a similar abstraction/beta-scission sequence can lead to acetylene. Methyl radicals can add to C_2 unsaturated species to form unsaturated C_3 species and so on, leading to formation of aromatics and ultimately to deposits. In this context, the changing concentrations in the gas channel as a result of the catalytic and electrochemical reactions within the anode have the potential to substantially affect the kinetics of molecular-weight growth.

Fig. 8a and b show the effects of reforming and electrochemistry on the gas-phase species profiles of CH_3, C_2H_6, for the case of 20% methane mole fraction in the inlet stream. Profiles are shown for gas-phase chemistry alone, open-circuit voltage, and $E_{cell} = 0.8$ V. In all cases, the inlet flow rates are the same. From Fig. 7b, it is apparent that catalytic reforming chemistry consumes CH_4. This, in turn, causes a decrease in CH_3, as can be seen in Fig. 8a. The decrease in CH_3 is important because CH_3 recombination ($CH_3 + CH_3 \rightleftharpoons C_2H_6$) is the first step toward molecular-weight growth. It can be seen from Fig. 8b that a decrease in methyl radicals causes a decrease in C_2H_6. As a result of reduced C_2H_6 levels, there is decreased production of unsaturated species like ethylene and acetylene, which ultimately leads to a decreased propensity for deposit formation.

The propensity for deposit formation can be characterized in terms of the net mole fraction of all species containing five or more carbon atoms (designated as C_{5+}). This definition is adequate to relate the temperature dependence of the observed deposit formation in butane and ethanol pyrolysis to that observed experimentally [16,32]. Interestingly, Fig. 8c shows that catalytic reforming and electrochemical activity tends to reduce the C_{5+} levels relative to gas-phase chemistry alone. However, compared to reforming alone, electrochemical activity tends to increase the C_{5+} levels, and hence the deposit propensity. Increased H_2O levels via electrochemical reaction increases the OH radicals concentration produced in the gas phase. This increase in the radical pool leads to more rapid conversion of ethane to unsaturates such as C_2H_2, which in turn leads to increased molecular-weight growth.

Despite the chemical insight derived from this analysis, it is important to note that for all the cases considered in this paper the C_{5+} levels are far below those where deposits might be formed

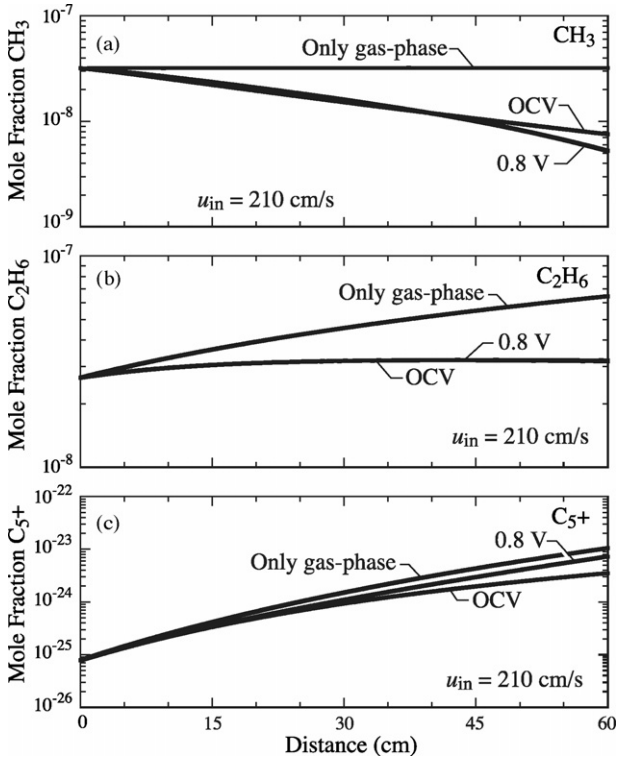

Fig. 8. Predicted mole fractions of (a) CH_3, (b) C_2H_6, and (c) C_{5+} at 800 °C and 1 atm. Fuel inlet composition is 10.6% CH_4, 47.0% H_2O, 28.6% H_2, 12.4% CO_2, and 1.4% CO, corresponding to a 20% CH_4 fraction. Fuel utilization is 85% for the $E_{cell} = 0.8$ V case and inlet flow rates for all cases are the same.

via gas-phase routes. A general guideline is that C_{5+} mole fractions must be in the range of 10^{-3} before deposits are observed [16]. The cases studied in this paper all considered upstream steam reforming with steam–carbon ratios of 3. Because these conditions were chosen specifically to avoid deposit formation, it is reassuring that the analysis predicts very low propensity for molecular-weight growth.

8. Summary and conclusions

We have simulated and analyzed a tubular SOFC fed by an upstream JP-8 steam reformer. The reformer, which is operated at a steam–carbon ratio of 3, is assumed to deliver a reformate stream that is at chemical equilibrium at the reformer temperature. By varying the reformer temperature, the methane mole fraction in the reformate stream is varied from 0 to 20% (on a dry basis). These reformate streams are used as input to a fuel-cell model that predicts local variables, such as species composition and local heat release throughout the cell. The fuel-cell model also predicts global metrics, such as efficiency and power density.

Increasing the CH_4 fraction in the reformate leads to increased fuel-cell efficiency, but decreased power density. Fuel-cell efficiency is highest at operating potentials around 0.8 V, while power densities are highest at operating potentials around 0.6 V. Increased methane mole fraction in the fuel stream tends to make the local heat-release profiles more uniform, which is generally beneficial at the cell level.

The model is used to explore the influence of electrochemistry and heterogeneous reforming kinetics on gas-phase kinetics and the propensity for polyaromatic deposit formation. Because of the very high computational cost of including full gas-phase kinetics (i.e., 3450 reactions) in the fuel-cell models, a two-step decoupled approach is used. A fuel-cell model that neglects gas-phase kinetics (but does include detailed heterogeneous reforming kinetics) is used to predict major-species flux exchange between a porous anode structure and the fuel flow channel. These fluxes are then imposed on a fuel-channel model that considers the full gas-phase kinetics.

Although gas-phase kinetics is found to be negligible for the highly reformed fuel streams considered in this paper, the modeling approaches and chemical insight are valuable. There is growing effort in the SOFC community to reduce or eliminate upstream reforming, and to introduce higher hydrocarbons directly into the anode flow channels. In these cases, with internal reforming or partial oxidation, gas-phase kinetics is expected to play a much larger role.

Acknowledgements

This work was supported by the Office of Naval Research under grants N00014-02-1-0665 (DoD Multidisciplinary University Research Initiative (MURI)) and N00014-05-1-0339 (Research Tools Consortium). Aspects of the JP-8 reforming analysis were supported by N00014-05-M-0198 (InnovaTek as prime contractor).

References

[1] A. Weber, B. Sauer, A. Müller, D. Herbstritt, E. Ivers-Tiffée, Oxidation of H_2, CO and methane in SOFCs with Ni/YSZ-cermet anodes, Solid State Ionics 152–153 (2002) 543–550.
[2] E. Murray, T. Tsai, S. Barnett, A direct-methane fuel cell with a ceria-based anode, Nature 400 (1999) 649–651.
[3] G. Saunders, K. Kendall, Reactions of hydrocarbons in small tubular SOFCs, J. Power Sources 106 (2002) 258–263.
[4] H. Kim, S. Park, J. Vohs, R. Gorte, Direct oxidation of liquid fuels in a solid oxide fuel cell, J. Electrochem. Soc. 148 (2001) A693–A695.
[5] J. Wang, J.-C. Jang, T.-J. Huang, Study of Ni-samaria-doped ceria anode for direct oxidation of methane in solid oxide fuel cells, J. Power Sources 122 (2003) 122–131.
[6] J. Liu, S. Barnett, Operation of anode-supported solid oxide fuel cells on methane and natural gas, Solid State Ionics 158 (2003) 11–16.
[7] K. Kendall, C. Finnerty, G. Saunders, J. Chung, Effects of dilution on methane entering an SOFC anode, J. Power Sources 106 (2002) 323–327.
[8] S. Livermore, J. Cotton, R. Ormerod, Fuel reforming and electrical performance studies in intermediate temperature ceria-gadolinia-based SOFCs, J. Power Sources 86 (2000) 411–416.
[9] S. McIntosh, H. He, S.-I. Lee, O. Costa-Nunes, V. Krishnan, J. Vohs, R. Gorte, An examination of carbonaceous deposits in direct-utilization SOFC anodes, J. Electrochem. Soc. 151 (2004) A604–A608.
[10] Y. Jiang, A. Virkar, A high performance, anode-supported solid oxide fuel cell operating on direct alcohol, J. Electrochem. Soc. 148 (2001) A706–A709.
[11] Z. Zhan, J. Liu, S. Barnett, Operation of anode-supported solid oxide fuel cells on propane air fuel mixtures, Appl. Catal. A 262 (2004) 255–259.
[12] T. Kim, G. Liu, M. Boaro, S.-I. Lee, J. Vohs, R. Gorte, A study of carbon formation and prevention in hydrocarbon-fueled SOFC, J. Power Sources 155 (2006) 231–238.

[13] S. McIntosh, R. Gorte, Direct hydrocarbon SOFC, Chem. Rev. 104 (2004) 4845–4865.
[14] B. Monnerat, L. Kiwi-Minsker, A. Renken, Hydrogen production by catalytic cracking of methane over nickel gauze under periodic reactor operation, Chem. Eng. Sci. 56 (2001) 633–639.
[15] T. Zhang, M. Amiridis, Hydrogen production via the direct cracking of methane over silica-supported nickel catalysts, Appl. Catal. A 167 (1998) 161–172.
[16] C. Sheng, A. Dean, The importance of gas phase kinetics within the anode channel of a solid-oxide fuel cell, J. Phys. Chem. A 108 (2004) 3772–3783.
[17] C. Goralski, R. O'Connor, L. Schmidt, Modeling homogeneous and heterogeneous chemistry in the production of syngas from methane, Chem. Eng. Sci. 55 (2000) 1357–1370.
[18] J.-W. Snoeck, G. Froment, M. Fowles, Steam/CO_2 reforming of methane. Carbon formation and gasification on catalysts with various potassium contents, Ind. Eng. Chem. Res. 41 (2002) 3548–3556.
[19] S. Clarke, A. Dicks, K. Pointon, T. Smith, A. Swann, Catalytic aspects of the steam reforming of hydrocarbons in internal reforming fuel cells, Catal. Today 38 (1997) 411–423.
[20] F. Coutelieris, S. Douvartzides, P. Tsiakaras, The importance of the fuel choice on the efficiency of a solid oxide fuel cell system, J. Power Sources 123 (2003) 200–205.
[21] H. Zhu, A.M. Colclasure, R.J. Kee, Y. Lin, S.A. Barnett, Anode barrier layers for tubular solid-oxide fuel cells with hydrocarbon fuel streams, J. Power Sources, in press.
[22] H. Zhu, R. Kee, V. Janardhanan, O. Deutschmann, D. Goodwin, Modeling elementary heterogeneous chemistry and electrochemistry in solid-oxide fuel cells, J. Electrochem. Soc. 152 (2005) A2427–A2440.
[23] E. Hecht, G. Gupta, A. Dean, H. Zhu, R. Kee, Methane reforming kinetics within a Ni-YSZ SOFC anode, Appl. Catal. A: Gen. 295 (2005) 40–51.
[24] G. Gupta, A. Dean, E. Hecht, H. Zhu, R. Kee, Gas-phase reactions of methane and natural gas with air and steam in the non-catalytic channels of a solid-oxide fuel cell, J. Power Sources 156 (2006) 434–447.
[25] Y. Jiang, A. Virkar, Fuel composition and diluent effect on gas transport and performance of anode-supported SOFCs, J. Electrochem. Soc. 150 (2003) A942–A951.
[26] R. Kee, F. Rupley, E. Meeks, J. Miller, CHEMKIN-III: A FORTRAN chemical kinetics package for the analysis of gas phase and plasma kinetics, Tech. Re SAND96–8216, Sandia National Laboratories, 1996.
[27] P. Brown, G. Byrne, A. Hindmarsh, VODE: a variable coefficient ode solver, SIAM J. Sci. Stat. Comput. 10 (1989) 1038–1051.
[28] J.J. Strohm, J. Zheng, C. Song, Low-temperature steam reforming of jet fuel in the absence and presence of sulfur over Rh and Rh-Ni catalysts for fuel cells, J. Catal. 238 (2006) 309–320.
[29] B. Thorstensen, A parametric study of fuel cell system efficiency under full and part load operation, J. Power Sources 92 (2001) 9–16.
[30] H. Zhu, R. Kee, Thermodynamics of SOFC efficiency and fuel utilization as functions of fuel mixtures and operating conditions, J. Power Sources, in press.
[31] P. Aguiar, D. Chadwick, L. Kershenbaum, Effect of methane slippage on an indirect internal reforming solid oxide fuel cell, Chem. Eng. Sci. 59 (2004) 87–97.
[32] G. Gupta, A. Dean, K. Ahn, R. Gorte, Comparison of conversion and deposit formation of ethanol and butane under SOFC conditions, J. Power Sources 158 (2006) 497–503.